



## RESEARCH ARTICLE

[View Article Online](#)  
[View Journal](#) | [View Issue](#)

 Cite this: *Inorg. Chem. Front.*, 2023,  
 10, 5694

# A surface-dynamic approach toward supercrystal engineering of titanium–oxo clusters†

 Ling-Cui Meng,<sup>‡</sup> Zhi-Ming Feng,<sup>‡</sup> Zhan-Guo Jiang \* and Cai-Hong Zhan \*

The controlled synthesis and structure determination of two titanium–oxo (Ti–O) clusters (Ti<sub>10</sub>Cu<sub>2</sub>)<sub>sp</sub> (sp: hard-sphere-like packing) and (Ti<sub>10</sub>Cu<sub>2</sub>)<sub>cs</sub> (cs: chain stacking) are presented. In contrast to the previously reported assemblies of Ti–O clusters by organic or inorganic linkers, (Ti<sub>10</sub>Cu<sub>2</sub>)<sub>sp</sub> and (Ti<sub>10</sub>Cu<sub>2</sub>)<sub>cs</sub> are achieved *via* regulating the surface dynamics of Ti–O clusters and further stabilized by CH⋯π interactions. The surface dynamics was regulated *via* a change of dynamically detached Sal-Cu/OMe-Cu motifs (Sal = salicylic acid). More importantly, benefiting from the difference in structures, (Ti<sub>10</sub>Cu<sub>2</sub>)<sub>cs</sub> exhibits excellent conductive properties and different photocatalytic activities.

 Received 13th July 2023,  
 Accepted 15th August 2023  
 DOI: 10.1039/d3qi01334k

[rsc.li/frontiers-inorganic](https://rsc.li/frontiers-inorganic)

In recent decades, the field of crystalline materials has seen significant expansion through the adoption of inorganic nanoparticles (NPs), which have remarkable size dependent properties, effectively enhancing the scope of the design and synthesis of materials.<sup>1</sup> Assembling monodisperse NPs into supercrystals has proved to be an effective way to modulate their intrinsic optical, electronic, magnetic and catalytic activities through interparticle coupling and crystal order coherence, which can be promoted by diverse interparticle interactions, including electrostatic interactions, depletion force,<sup>2</sup> metallophilicity,<sup>3</sup> hydrogen bonding<sup>4</sup> and biorecognition interactions.<sup>5</sup> The entire process, *i.e.*, the assembly of nanocrystals, atomic alignment, and unification by attachment, is very complex and intriguing.<sup>6</sup>

It is interesting to note that recent significant advancements in the synthesis, structural discovery, functionalization, and theoretical understanding of ligand-stabilized,<sup>7</sup> atom-precise metal nanoclusters and semiconductor clusters have created intriguing possibilities for implementing these precisely defined, nanometer-size building blocks to design nanomaterials with adjustable properties.<sup>8</sup> These atomically precise clusters are powerful model systems for establishing the precise structure composition–property correlation and understanding the physicochemical dynamic behaviors, both of

which are difficult or impossible to achieve in the traditional NP system.<sup>9</sup>

Titanium dioxide (TiO<sub>2</sub>) and related Ti–O nanomaterials have been widely applied as photocatalysts for light driven water splitting and the degradation of environmental pollutants.<sup>10</sup> In recent decades, crystalline Ti–O clusters with precise atomic position information have been increasingly studied as well-defined models for TiO<sub>2</sub>.<sup>11</sup> From the perspective of structural dimensions, the Ti–O clusters exist across the full dimensions from 0D nanoclusters to 1D chains,<sup>12</sup> 2D layers,<sup>13</sup> and 3D diamond frameworks,<sup>14</sup> which are bridged together by intercluster linkers such as organic or inorganic ligands.<sup>15</sup> However, there are few examples of the surface dynamics of Ti–O clusters regulating the structure (for example, size, shape and packing symmetry). The crystal packing not only depends on the strong coordination bond but is also influenced by noncovalent intermolecular interactions such as hydrogen bonds and van der Waals, π⋯π, and C–H⋯π interactions,<sup>16</sup> which can lead to the formation of multiple crystalline forms.<sup>17</sup>

The design and fabrication of the extended structures are not only critical for elucidating the fundamental molecular and thermodynamic principles that regulate the assembly processes, but they also provide the opportunity to modify the microscopic electronic structure, optical response,<sup>18</sup> and ultimate macroscopical performances. Herein, we demonstrated that the surface dynamics of Sal-Cu/OMe-Cu can serve to regulate the structure of the packing symmetry of Ti–O clusters. A new {Ti<sub>10</sub>Cu<sub>2</sub>} cluster was isolated and used as a model to regulate the surface dynamics *via* a change of dynamically detached Sal-Cu/OMe-Cu motifs (Fig. 1, central panels). In the presence of –OMe, {Ti<sub>10</sub>Cu<sub>2</sub>} tends to pack as hard spheres in hexagonal superlattices, forming a macroscopic block supercrystal shape (Fig. 1, top panels). However, the loss of a term-

Key Laboratory of the Ministry of Education for Advanced Catalysis Materials  
 Institute of Physical Chemistry, College of Chemistry and Materials Science,  
 Zhejiang Normal University, No. 688, Yingbin Avenue, Jinhua, Zhejiang, 321004,  
 China. E-mail: jzg@zjnu.cn, chzhan@zjnu.cn

†Electronic supplementary information (ESI) available. CCDC 2277134 and 2277142. For ESI and crystallographic data in CIF or other electronic format see DOI: <https://doi.org/10.1039/d3qi01334k>

‡These authors contributed equally to this work.

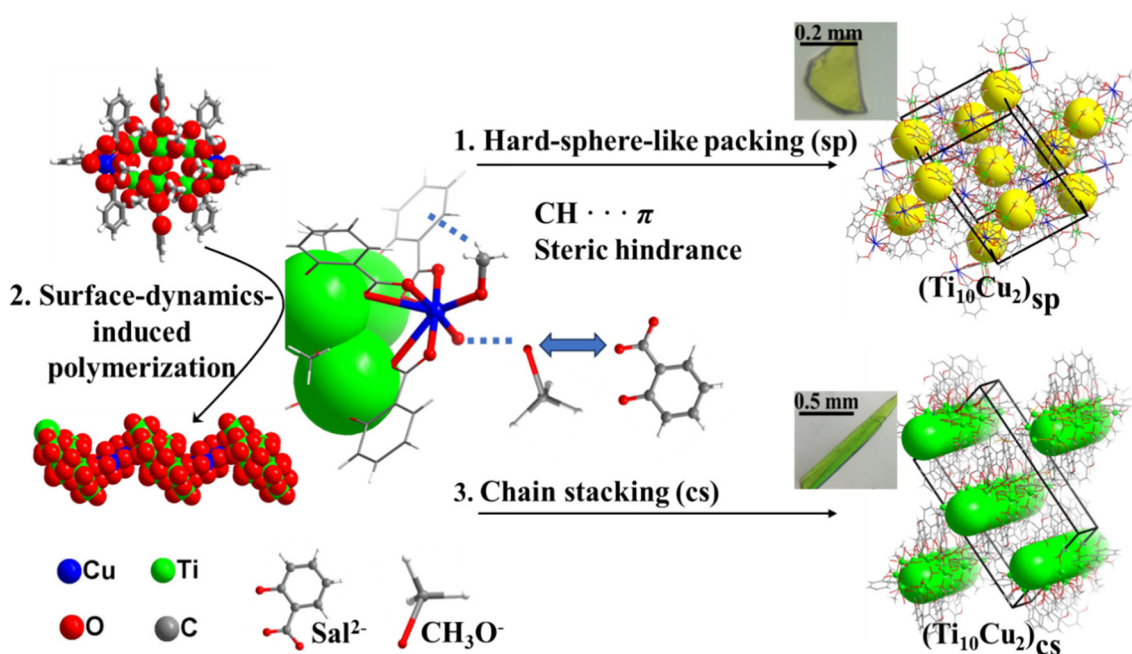


**Fig. 1** Schematic illustration of the crystallization of  $\{Ti_{10}Cu_2\}$  into either hexagonal superlattices and block crystals (top) or, in the absence of one terminal  $-OMe$ , rod-like supercrystals (bottom). The  $OMe-Cu$  fragments dynamically detached from  $\{Ti_{10}Cu_2\}$  clusters and  $Sal-Cu$  fragments are grafted to  $\{Ti_{10}Cu_2\}$  clusters to favour 1D alignment of the clusters.

inal  $-OMe$  will give rise to polymers connected by  $Sal-Cu$  linkers. The packing of the as-formed polymers leads to micrometre-sized rod-like supercrystals (Fig. 1, bottom panels). The packing symmetry and morphology of  $\{Ti_{10}Cu_2\}$  can be tuned by the surface dynamics of  $Sal-Cu/OMe-Cu$ . This work demonstrates a facile method for engineering the morphology and symmetry of crystalline nanocluster metamaterials in the micrometre-size regime and highlights the importance of the surface dynamics of nanoclusters in determining their assembly behaviour.

The syntheses of  $[H_6Ti_{10}Cu_2(\mu_2-O)_6(\mu_3-O)_2(sal)_8(OCH_3)_{18}]$  (denoted as  $(Ti_{10}Cu_2)_{sp}$ ) and  $[H_4Ti_{10}Cu_2(\mu_2-O)_6(\mu_3-O)_2(sal)_8(OCH_3)_{16}]$  (denoted as  $(Ti_{10}Cu_2)_{cs}$ ) are summarized in Fig. S1–S3.† Through the solvothermal reaction of salicylic acid,  $Ti(O^iPr)_4$  and  $CuCl_2 \cdot 2H_2O$  in  $CH_3OH$  at 60 °C for 48 h, yellow block crystals of  $(Ti_{10}Cu_2)_{sp}$  were obtained. Single-crystal analysis shows that  $(Ti_{10}Cu_2)_{sp}$  crystallizes in the  $P2_1/c$  space group, and the cluster consists of 10  $Ti(IV)$  and 8  $Sal^{2-}$  ligands. Every four  $Ti(IV)$  are connected by two  $\mu_3-O$  to generate a trapezoidal  $\{Ti_4\}$  unit, and two parallel  $\{Ti_4\}$  trapezoids are further bridged by four  $\mu_2-O$  to form a  $\{Ti_8\}$  double layer. The remaining two  $Ti(IV)$  and two  $Cu(II)$  are connected by  $Sal^{2-}$  to generate two pairs of  $\{TiCu\}$  dimers, which are attached to the  $\{Ti_8\}$  core from the side of the double layer. The  $Sal^{2-}$  ligands exhibit two different coordination fashions: two ligands, each of which bridges two  $Ti(IV)$  in the  $\{Ti_8\}$  core through the carboxylic group, and the remaining six  $Sal^{2-}$  ligands, each of which connects one  $Ti(IV)$  cation and one  $Cu(II)$  with its carboxylic groups and then continues to bridge one  $Ti(IV)$  cation through its hydroxy group. Both  $Cu(II)$  are eight-coordinated,

and the coordination sphere is defined by three carboxylic  $COO^-$  and two  $CH_3O^-$  anions. Furthermore, another  $Ti-O$  cluster  $(Ti_{10}Cu_2)_{cs}$  was achieved by increasing the concentration of the starting materials. Unlike  $(Ti_{10}Cu_2)_{sp}$ ,  $(Ti_{10}Cu_2)_{cs}$  features a 1D chain.

As shown in Fig. 2a, in the hard-sphere-like packing pattern,  $-OMe$  undergoes  $CH \cdots \pi$  interactions with two  $Sal^{2-}$  ligands of the adjacent  $\{Ti_{10}Cu_2\}$  clusters (Fig. 2b and c). The arrangement of  $\{Ti_{10}Cu_2\}_{sp}$  can be formed by close packing in an ABAB stacking manner (Fig. S4†). The  $Cu-O$  bond length varies from 1.959 to 2.863 Å (av. 2.255 Å) in  $(Ti_{10}Cu_2)_{sp}$  and from 1.954 to 2.842 Å (av. 2.379 Å) in  $(Ti_{10}Cu_2)_{cs}$ , respectively. These changes are seemingly subtle; however, they are the origin of different packing patterns of the crystal. To be specific, in  $(Ti_{10}Cu_2)_{sp}$ , the bond lengths of  $Cu-O$  (derived from  $-OMe$ ) are 2.0694 Å and 2.1819 Å (Fig. S5†). During chain stacking,  $\{Ti_{10}Cu_2\}$  lost a terminal  $-OMe$ . Then the adjacent  $\{Ti_{10}Cu_2\}$  clusters are further extended to 1D chains through two  $Sal-Cu$  motifs (Fig. 2e). As a result, each  $\{Ti_{10}Cu_2\}$  cluster unit in the polymer has two linker hinges attached to it as shown in Fig. 2d. Compared with  $(Ti_{10}Cu_2)_{sp}$ , the bond lengths of  $Cu-O$  (derived from  $-OOC$  and  $-OMe$ ) are 2.7080 Å and 1.9544 Å (Fig. S6†), respectively. The remaining bond lengths of  $Cu-O$  are listed in Table S2.† In  $(Ti_{10}Cu_2)_{sp}$ , the angles of  $Cu-O-C$  are 134.655° and 118.907°. Upon transformation to the polymer, the  $Cu-O-C$  angle of the linker is changed. In  $(Ti_{10}Cu_2)_{cs}$ , the angles are 142.429° and 121.529° (Table S2†). Furthermore, the angles between planes composed of  $Sal^{2-}$  ligands coordinated with copper are also different. The angles between the planes of ligand A and ligand B are 82.603° and

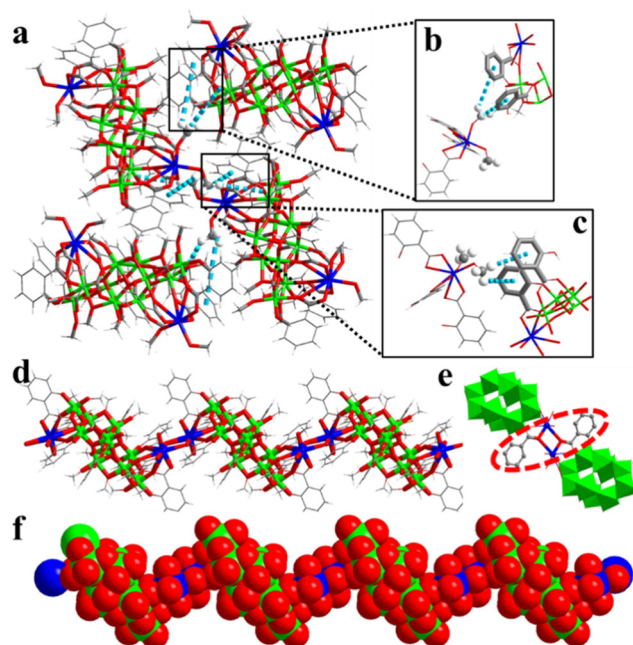


**Fig. 2** In  $(\text{Ti}_{10}\text{Cu}_2)_{\text{sp}}$ , the  $\text{CH}\cdots\pi$  interactions of inter-clusters between  $\text{Sal}^{2-}$  ligands and  $-\text{OMe}$  (a). (b and c) Enlarged view of the area outlined in (a). In  $(\text{Ti}_{10}\text{Cu}_2)_{\text{cs}}$ , view of the chain structure (d), "Sal-Cu" units (e) and space-filling view of the chain (f). Colour code and representation: Ti, green; Cu, blue; O, red; C, grey; H, white;  $\text{CH}\cdots\pi$  interactions, dashed cyan lines.

$82.370^\circ$ , respectively (Fig. S7 and S8<sup>†</sup>). In addition, the angles between the planes of ligand A and ligand C are  $1.649^\circ$  and  $14.420^\circ$ , respectively (Fig. S9 and S10<sup>†</sup>). There are  $\text{CH}\cdots\pi$  interactions of the  $\{\text{Ti}_{10}\text{Cu}_2\}$  intrachain between the  $-\text{OMe}$  and the ligands (Fig. S11<sup>†</sup>). For  $(\text{Ti}_{10}\text{Cu}_2)_{\text{cs}}$ , there are also  $\text{CH}\cdots\pi$  interactions of intrachains (Fig. S12<sup>†</sup>). In short, the difference in steric hindrance and the presence of  $\text{CH}\cdots\pi$  interactions together contribute to the distinguishing assembly of  $\{\text{Ti}_{10}\text{Cu}_2\}$  clusters.

The XRD patterns of the two superlattices match well with the simulated ones, verifying the phase purity. The differences in intensity may be due to the preferred orientation of the powder samples (Fig. S13 and S14<sup>†</sup>). The IR spectra reveal the  $\nu_{\text{as}}(\text{COO}^-)$  vibration of the carboxylic groups and also the typical vibrations for Ti-O (Fig. S15 and S16<sup>†</sup>).<sup>10b</sup> Thermogravimetric analysis (TGA) experiments show continuous weight loss from room temperature to  $300^\circ\text{C}$ , corresponding to the elimination of coordinated solvent molecules, after which the structures begin to decompose thermally (Fig. S17 and S18<sup>†</sup>). The UV-vis spectra of  $(\text{Ti}_{10}\text{Cu}_2)_{\text{sp}}$  and  $(\text{Ti}_{10}\text{Cu}_2)_{\text{cs}}$  in  $\text{CHCl}_3$  show the same bands at 310 nm and 365 nm (Fig. 3). It is speculated that breakdown of the polymer occurs in solution, leading to the formation of the molecular nanocluster.

In the single crystal, the polymeric chains of  $(\text{Ti}_{10}\text{Cu}_2)_{\text{cs}}$  are stacked parallelly in a unit cell, exhibiting a highly anisotropic crystal shape. The electrical conductivity, measured from the slope of the linear  $I$ - $V$  curve, was found to be  $5.9 \times 10^{-9} \text{ S m}^{-1}$

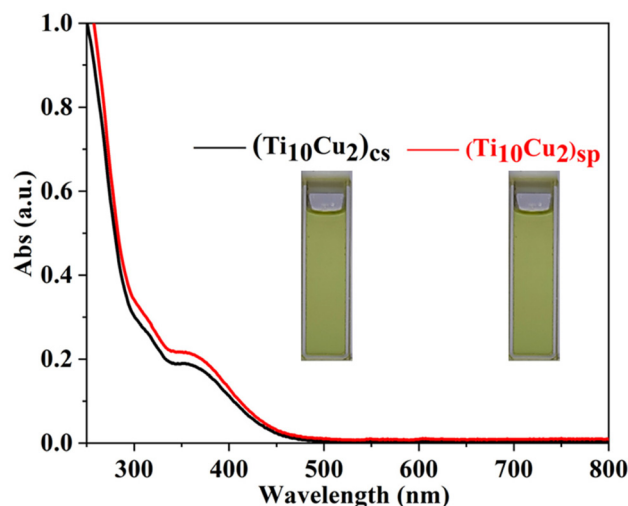


**Fig. 3** UV spectra of  $(\text{Ti}_{10}\text{Cu}_2)_{\text{cs}}$  and  $(\text{Ti}_{10}\text{Cu}_2)_{\text{sp}}$  in chloroform.

for the polymeric crystal at room temperature (Fig. 4a). Comparatively, the conductivity of  $(\text{Ti}_{10}\text{Cu}_2)_{\text{sp}}$  crystals is lower, around  $4.1 \times 10^{-10} \text{ S m}^{-1}$  (Fig. 4b). Such a notable change in electrical conductivity may arise from the variant configurations of the  $\text{CH}\cdots\pi$  interaction of the surface hooks, which are composed of  $\text{Sal}^{2-}$  ligands and  $-\text{OMe}$ . Blank controls without crystal samples were also measured, showing only instrument noise levels (Fig. S23<sup>†</sup>), which means that the conductivity is contributed by the crystal material itself. These results demonstrate that the direct linkage of clusters using Sal-Cu is advantageous for carrier transport.

The electronic band structures of the two superlattices were investigated using UV-vis DRS and Mott-Schottky measurements. As shown in Fig. S19<sup>†</sup>,  $(\text{Ti}_{10}\text{Cu}_2)_{\text{sp}}$  and  $(\text{Ti}_{10}\text{Cu}_2)_{\text{cs}}$  display similar adsorption profiles in the wavenumber range of 200–800 nm. The Tauc plot determines the optical band gaps of  $(\text{Ti}_{10}\text{Cu}_2)_{\text{sp}}$  and  $(\text{Ti}_{10}\text{Cu}_2)_{\text{cs}}$  to be 2.27 eV and 2.35 eV, respectively, indicating that the band gap ( $E_g$ ) values of the two superlattices are not significantly altered, with a small difference of only 0.08 eV (Fig. S20<sup>†</sup>). Mott-Schottky plots were obtained for three different frequencies (1000 Hz, 1300 Hz, and 1500 Hz) to verify the lowest unoccupied molecular orbital (LUMO) energy levels of  $(\text{Ti}_{10}\text{Cu}_2)_{\text{sp}}$  and  $(\text{Ti}_{10}\text{Cu}_2)_{\text{cs}}$ , resulting

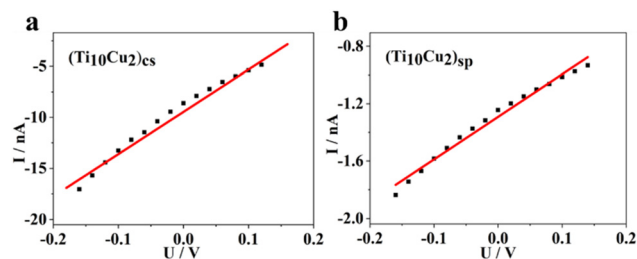


**Fig. 4** The conductance of  $(\text{Ti}_{10}\text{Cu}_2)_{\text{cs}}$  (a) and  $(\text{Ti}_{10}\text{Cu}_2)_{\text{sp}}$  (b) ranging from  $-0.2 \text{ V}$  to  $0.2 \text{ V}$ .

in values of  $-0.47$  V vs. NHE and  $-0.67$  V vs. NHE, respectively (Fig. 5a and b). Based on the results of the band gaps and Mott–Schottky plots, the band structure diagrams of  $(\text{Ti}_{10}\text{Cu}_2)_{\text{sp}}$  and  $(\text{Ti}_{10}\text{Cu}_2)_{\text{cs}}$  were obtained.

Although Ti–O clusters with different structures and electronic properties have been characterized in a report, which mainly focuses on photocatalytic water splitting and dye degradation, investigations on  $\text{CO}_2$  photoreduction applications still remain rare.<sup>19</sup> The  $\text{CO}_2$  photoreduction experiments of  $(\text{Ti}_{10}\text{Cu}_2)_{\text{cs}}$  and  $(\text{Ti}_{10}\text{Cu}_2)_{\text{sp}}$  were explored to evaluate the efficiency of  $\text{CO}_2$  reduction catalysis, with all experimental details documented in the ESI.† The  $(\text{Ti}_{10}\text{Cu}_2)_{\text{cs}}$  catalyst was demonstrated to have a higher efficacy of  $\text{CO}_2$  reduction to  $\text{CH}_4$  due to its well-matched band structure and reduction sites. Notably, the reduction product  $\text{CO}$  was only observed on the  $(\text{Ti}_{10}\text{Cu}_2)_{\text{cs}}$  catalyst, which can be attributed to its lower LUMO energy level required for  $\text{CO}_2$  to  $\text{CO}$  photoreduction, necessitating more negative reduction potential (Fig. 5c and d). With the increasing irradiation time, the yields of  $\text{CO}$  and  $\text{CH}_4$  increase simultaneously at different reaction rates; the amounts of  $\text{CH}_4$  and  $\text{CO}$  for  $(\text{Ti}_{10}\text{Cu}_2)_{\text{cs}}$  reached up to 44.5 and 97.4  $\mu\text{mol g}^{-1}$  after 4 h. In contrast, only  $\text{CH}_4$  production of  $(\text{Ti}_{10}\text{Cu}_2)_{\text{sp}}$  was achieved after 4 h of irradiation, and the amount of  $\text{CH}_4$  for  $(\text{Ti}_{10}\text{Cu}_2)_{\text{sp}}$  reached up to 46.5  $\mu\text{mol g}^{-1}$ .

$(\text{Ti}_{10}\text{Cu}_2)_{\text{cs}}$  and  $(\text{Ti}_{10}\text{Cu}_2)_{\text{sp}}$  are also comparable to existing semiconducting materials such as Ti/Cu-based nanomaterials (Table S3,† entries 1–18) and metal–oxygen clusters (Table S3,† entries 19–21). Compared with some nano-sized semiconductors,  $(\text{Ti}_{10}\text{Cu}_2)_{\text{cs}}$  and  $(\text{Ti}_{10}\text{Cu}_2)_{\text{sp}}$  exhibit lower photocatalytic performance to produce  $\text{CO}$ , while higher photocatalytic performance to produce  $\text{CH}_4$ , and show much better photocatalytic activity compared with metal–oxygen clusters. What's more, this work provides new ideas for the structural design, synthesis and application of cluster-based functional

materials and also sets up a model for effective electron transfer in catalytic applications. The experimental conditions confirmed that light and catalysts are mandatory for  $\text{CO}_2$  reduction, as no gas production was observed in the absence of light or catalysts. The efficiency of photoinduced electron transfer was analysed using a transient short-circuit photocurrent response test (Fig. S24†), demonstrating rapid photocurrent generation upon turning on the light with rapid decay after light cessation, indicating excellent photocurrent response for  $(\text{Ti}_{10}\text{Cu}_2)_{\text{cs}}$ .

In conclusion, two novel superlattices were synthesized using a new nanocluster  $\{\text{Ti}_{10}\text{Cu}_2\}$  as a molecular building block. The single crystal X-ray analysis of the nanocluster superstructure provides detailed structural information about the building block, the linker, and the packing patterns. The hard-sphere-like packing  $(\text{Ti}_{10}\text{Cu}_2)_{\text{sp}}$  and chain stacking  $(\text{Ti}_{10}\text{Cu}_2)_{\text{cs}}$  are achieved *via* regulating dynamically the surface Sal-Cu/OMe-Cu motifs of  $\{\text{Ti}_{10}\text{Cu}_2\}$ .  $(\text{Ti}_{10}\text{Cu}_2)_{\text{cs}}$  exhibits excellent electrical conductivity and photocurrent response and efficacy of  $\text{CO}_2$  reduction to  $\text{CO}$ . This study sheds light on the fundamental structure–property relationships in cluster-based networks and introduces a new avenue for investigating a family of semiconductor cluster assemblies.

## Conflicts of interest

There are no conflicts to declare.

## Acknowledgements

This work was supported by the National Natural Science Foundation of China (NSFC 21801226), the Natural Science Foundation of Zhejiang Province (LY20B010002 and LQ22B010002) and the Zhejiang Normal University Fund.

## Notes and references

- (a) C. J. Zeng, Y. X. Chen, K. Kirschbaum, K. J. Lambright and R. C. Jin, Emergence of hierarchical structural complexities in nanoparticles and their assembly, *Science*, 2016, **354**, 1580; (b) A. M. Kalsin, M. Fialkowski, M. Paszewski, S. K. Smoukov, K. J. M. Bishop and B. A. Grzybowski, Electrostatic self-assembly of binary nanoparticle crystals with a diamond-like lattice, *Science*, 2006, **312**, 420; (c) R. W. Huang, Y. S. Wei, X. Y. Dong, X. H. Wu, C. X. Du, S. Q. Zang and T. C. W. Mak, Hypersensitive dual-function luminescence switching of a silver-chalcogenolate cluster-based metal–organic framework, *Nat. Chem.*, 2017, **9**, 689; (d) S. Takano and T. Tsukuda, Chemically modified gold/silver superatoms as artificial elements at nanoscale: Design principles and synthesis challenges, *J. Am. Chem. Soc.*, 2021, **143**, 1683; (e) E. V. Shevchenko, D. V. Talapin, N. A. Kotov, S. O'Brien and C. B. Murray, Structural diver-

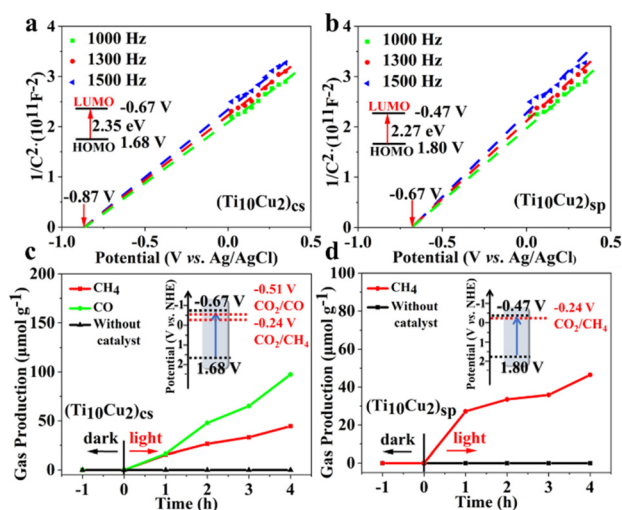


Fig. 5 Mott–Schottky plots of  $(\text{Ti}_{10}\text{Cu}_2)_{\text{cs}}$  (a) and  $(\text{Ti}_{10}\text{Cu}_2)_{\text{sp}}$  (b). Time courses of photocatalytic  $\text{CO}_2$  reduction using  $(\text{Ti}_{10}\text{Cu}_2)_{\text{cs}}$  (c),  $(\text{Ti}_{10}\text{Cu}_2)_{\text{sp}}$  (d) and their band structure diagrams.

- sity in binary nanoparticle superlattices, *Nature*, 2006, **439**, 55.
- M. I. Bodnarchuk, M. V. Kovalenko, W. Heiss and D. V. Talapin, Energetic and entropic contributions to self-assembly of binary nanocrystal superlattices: Temperature as the structure-directing factor, *J. Am. Chem. Soc.*, 2010, **132**, 11967.
  - (a) M. De Nardi, S. Antonello, D. E. Jiang, F. F. Pan, K. Rissanen, M. Ruzzi, A. Venzo, A. Zoleo and F. Maran, Gold nanowired: A linear  $(\text{Au}_{25})_n$  polymer from  $\text{Au}_{25}$  molecular clusters, *ACS Nano*, 2014, **8**, 8505; (b) S. Hossain, Y. Imai, Y. Motohashi, Z. H. Chen, D. Suzuki, T. Suzuki, Y. Kataoka, M. Hirata, T. Ono, W. Kurashige, T. Kawawaki, T. Yamamoto and Y. Negishi, Understanding and designing one-dimensional assemblies of ligand-protected metal nanoclusters, *Mater. Horiz.*, 2020, **7**, 796.
  - A. Desireddy, B. E. Conn, J. S. Guo, B. Yoon, R. N. Barnett, B. M. Monahan, K. Kirschbaum, W. P. Griffith, R. L. Whetten, U. Landman and T. P. Bigioni, Ultrastable silver nanoparticles, *Nature*, 2013, **501**, 399.
  - (a) Y. Tian, Y. G. Zhang, T. Wang, H. L. Xin, H. L. Li and O. Gang, Lattice engineering through nanoparticle–DNA frameworks, *Nat. Mater.*, 2016, **15**, 654; (b) M. B. Ross, J. C. Ku, V. M. Vaccarezza, G. C. Schatz and C. A. Mirkin, Nanoscale form dictates mesoscale function in plasmonic DNA–nanoparticle superlattices, *Nat. Nanotechnol.*, 2015, **10**, 453.
  - A. Ghosh, O. F. Mohammed and O. M. Bakr, Atomic-level doping of metal clusters, *Acc. Chem. Res.*, 2018, **51**, 3094.
  - Z. Lei, X. K. Wan, S. F. Yuan, Z. J. Guan and Q. M. Wang, Alkynyl approach toward the protection of metal nanoclusters, *Acc. Chem. Res.*, 2018, **51**, 2465.
  - (a) J. Z. Yan, B. K. Teo and N. F. Zheng, Surface chemistry of atomically precise coinage-metal nanoclusters: From structural control to surface reactivity and catalysis, *Acc. Chem. Res.*, 2018, **51**, 3084; (b) M. R. Friedfeld, J. L. Stein, A. Ritchhart and B. M. Cossairt, Conversion reactions of atomically precise semiconductor clusters, *Acc. Chem. Res.*, 2018, **51**, 2803; (c) J. X. Zhang, X. H. Bu, P. Y. Feng and T. Wu, Metal chalcogenide supertetrahedral clusters: Synthetic control over assembly, dispersibility, and their functional applications, *Acc. Chem. Res.*, 2020, **53**, 2261; (d) Z. Lei, J. J. Li, Z. A. Nan, Z. G. Jiang and Q. M. Wang, Cluster from cluster: A quantitative approach to magic gold nanoclusters  $[\text{Au}_{25}(\text{SR})_{18}]^-$ , *Angew. Chem., Int. Ed.*, 2021, **60**, 14415; (e) W. H. Wu, H. M. Zeng, Z. N. Yu, C. Wang, Z. G. Jiang and C. H. Zhan, Unusual structural transformation and luminescence response of magic-size silver(I) chalcogenide clusters via ligand-exchange, *Chem. Commun.*, 2021, **57**, 13337; (f) W. H. Wu, Y. Q. Gao, Y. F. Lin, Y. Y. Yuan, C. H. Zhan and Z. G. Jiang, The mystery of  $\text{Ph}_3\text{P}=\text{S}$  revealed in magic-size Ag–S cluster nucleation, *Dalton Trans.*, 2022, **51**, 17145.
  - P. Chakraborty, A. Nag, A. Chakraborty and T. Pradeep, Approaching materials with atomic precision using supra-molecular cluster assemblies, *Acc. Chem. Res.*, 2019, **52**, 2.
  - (a) Z. Zhao, X. Y. Zhang, G. Q. Zhang, Z. Y. Liu, D. Qu, X. Miao, P. Y. Feng and Z. C. Sun, Effect of defects on photocatalytic activity of rutile  $\text{TiO}_2$  nanorods, *Nano Res.*, 2015, **8**, 4061; (b) Y. X. Wu, X. R. Liu, G. Chen, Y. Q. Tian, J. Yan, X. Y. Yi and C. Liu, Cd-doped polyoxotitanium nanoclusters with a modifiable organic shell for photoelectrochemical water splitting, *Inorg. Chem.*, 2021, **60**, 19263.
  - (a) M. Y. Gao, F. Wang, Z. G. Gu, D. X. Zhang, L. Zhang and J. Zhang, Fullerene-like polyoxotitanium cage with high solution stability, *J. Am. Chem. Soc.*, 2016, **138**, 2556; (b) W. H. Fang, L. Zhang and J. Zhang, A 3.6 nm  $\text{Ti}_{52}$ -oxo nanocluster with precise atomic structure, *J. Am. Chem. Soc.*, 2016, **138**, 7480; (c) G. Y. Zhang, C. Y. Liu, D. L. Long, L. Cronin, C. H. Tung and Y. F. Wang, Water-soluble pentagonal-prismatic titanium-oxo clusters, *J. Am. Chem. Soc.*, 2016, **138**, 11097.
  - (a) S. Chen, N. Narayanam, L. Zhang and J. Zhang, Hydrogen bond-assisted homochiral lattice packing between inorganic helices built from heterometallic units, *Dalton Trans.*, 2018, **47**, 2134; (b) M. Albrecht, E. Isaak, M. Baumert, V. Gossen, G. Raabe and R. Fröhlich, “Induced fit” in chiral recognition: Epimerization upon dimerization in the hierarchical self-assembly of helicate-type titanium(IV) complexes, *Angew. Chem., Int. Ed.*, 2011, **50**, 2850.
  - (a) Y. F. Deng, S. D. Tang and S. P. Wu, Synthesis of calcium titanate from  $[\text{Ca}(\text{H}_2\text{O})_3]_2[\text{Ti}_2(\text{O}_2)_2\text{O}(\text{NC}_6\text{H}_6\text{O}_6)_2] \cdot 2\text{H}_2\text{O}$  as a cheap single-source precursor, *Solid State Sci.*, 2010, **12**, 339; (b) J. Dopta, S. Grzanna, C. Näther and W. Bensch, On the influence of the titanium source on the composition and structure of novel titanoniobates, *Dalton Trans.*, 2018, **47**, 15103.
  - (a) Y. J. Liu, W. H. Fang, L. Zhang and J. Zhang, Recent advances in heterometallic polyoxotitanium clusters, *Coord. Chem. Rev.*, 2020, **404**, 213099; (b) W. H. Fang, J. F. Wang, L. Zhang and J. Zhang, Titanium–oxo cluster based precise assembly for multidimensional materials, *Chem. Mater.*, 2017, **29**, 2681; (c) C. Wang, C. Liu, X. He and Z. M. Sun, A cluster-based mesoporous Ti-MOF with sodalite supercages, *Chem. Commun.*, 2017, **53**, 11670.
  - (a) Q. Li, J. C. Russell, T. Y. Luo, X. Roy, N. L. Rosi, Y. Zhu and R. C. Jin, Modulating the hierarchical fibrous assembly of Au nanoparticles with atomic precision, *Nat. Commun.*, 2018, **9**, 3871; (b) Z. R. Wen, Z. J. Guan, Y. Zhang, Y. M. Lin and Q. M. Wang,  $[\text{Au}_7\text{Ag}_9(\text{dppf})_3(\text{CF}_3\text{CO}_2)_7\text{BF}_4]_n$ : A linear nanocluster polymer from molecular  $\text{Au}_7\text{Ag}_8$  clusters covalently linked by silver atoms, *Chem. Commun.*, 2019, **55**, 12992; (c) P. Yuan, R. H. Zhang, E. Selenius, P. P. Ruan, Y. R. Yao, Y. Zhou, S. Malola, H. Hakkinen, B. K. Teo, Y. Cao and N. F. Zheng, Solvent-mediated assembly of atom-precise gold-silver nanoclusters to semiconducting one-dimensional materials, *Nat. Commun.*, 2020, **11**, 2229.
  - R. Taylor, Which intermolecular interactions have a significant influence on crystal packing?, *CrystEngComm*, 2014, **16**, 6852.
  - Q. F. Yao, L. M. Liu, S. Malola, M. Ge, H. Y. Xu, Z. N. Wu, T. K. Chen, Y. T. Cao, M. F. Matus, A. Pihlajamaki, Y. Han,

- H. Hakkinen and J. P. Xie, Supercrystal engineering of atomically precise gold nanoparticles promoted by surface dynamics, *Nat. Chem.*, 2023, **15**, 230.
- 18 (a) Z. Lei, X. L. Pei, Z. G. Jiang and Q. M. Wang, Cluster linker approach: Preparation of a luminescent porous framework with NbO topology by linking silver ions with gold(I) clusters, *Angew. Chem., Int. Ed.*, 2014, **53**, 12771; (b) K. Sheng, X. F. Tian, M. Jagodič, Z. Jagličić, N. Zhang, Q. Y. Liu, C. H. Tung and D. Sun, Synthesis, structure and magnetism of a novel  $\text{Cu}^{\text{II}}_4\text{Ti}^{\text{IV}}_5$  heterometallic cluster, *Chin. Chem. Lett.*, 2020, **31**, 809.
- 19 (a) W. H. Fang, L. Zhang and J. Zhang, Synthetic strategies, diverse structures and tuneable properties of polyoxo-titanium clusters, *Chem. Soc. Rev.*, 2018, **47**, 404; (b) M. Y. Gao, Z. Wang, Q. H. Li, D. Li, Y. Y. Sun, Y. H. Andaloussi, C. Ma, C. H. Deng, J. Zhang and L. Zhang, Black titanium-oxo clusters with ultralow band gaps and enhanced nonlinear optical performance, *J. Am. Chem. Soc.*, 2022, **144**, 8153; (c) N. Li, J. Liu, J. J. Liu, L. Z. Dong, S. L. Li, B. X. Dong, Y. H. Kan and Y. Q. Lan, Self-assembly of a phosphate-centered polyoxo-titanium cluster: Discovery of the heteroatom Keggin family, *Angew. Chem., Int. Ed.*, 2019, **58**, 17260; (d) K. Sheng, X. Q. Huang, R. Wang, W. Z. Wang, Z. Y. Gao, C. H. Tung and D. Sun, Decagram-scale synthesis of heterometallic Ag/Ti cluster as sustainable catalyst for selective oxidation of sulfides, *J. Catal.*, 2023, **417**, 185.